JOHNSON, C. K. (1970*a*). *Crystallographic Computing*, pp. 207–219. Copenhagen: Munksgaard.
JOHNSON, C. K. (1970*b*). *Thermal Neutron Diffraction*, pp. 132–160. Oxford Univ. Press.
JOHNSON, C. K. (1970*c*). *Crystallographic Computing*, pp. 220–226. Copenhagen: Munksgaard.
KENDALL, M. G. & STUART, A. (1969). *The Advanced Theory of Statistics*, Vol. I, ch. 3. London: Griffin.
PAWLEY, G. S. & WILLIS, B. T. M. (1970). *Acta Cryst.* A**26**, 260–262.
SCHERINGER, C. (1973). *Acta Cryst.* A**29**, 554–570.
SCHERINGER, C. (1977). *Acta Cryst.* A**33**, 879–884.
SCHERINGER, C., KUTOGLU, A. & MULLEN, D. (1978). *Acta Cryst.* A**34**, 481–483.
SCHOMAKER, V. & TRUEBLOOD, K. N. (1968). *Acta Cryst.* B**24**, 63–76.
WILLIS, B. T. M. & PAWLEY, G. S. (1970). *Acta Cryst.* A**26**, 254–259.

Acta Cryst. (1978). A**34**, 709–719

Experimental Study of Disordered Mica Structures by High-Resolution Electron Microscopy

BY SUMIO IIJIMA

Department of Physics, Arizona State University, Tempe, Arizona 85281, *USA*

AND PETER R. BUSECK

Departments of Geology and Chemistry, Arizona State University, Tempe, Arizona 85281, *USA*

(*Received* 3 *January* 1977; *accepted* 2 *March* 1978)

Disorder in stacking sequences of mica minerals, predominantly 1*M* muscovite from York, Ontario and biotite from Mitchell Co., North Carolina, was observed using high-resolution electron microscopy. The specimens were prepared by sectioning the flakes of mica in the microtome with a diamond knife, so that crystals were viewed down the direction parallel to the Si—O layers. Disordered sequences of the layers, as well as ordered crystals, are best described by citing the positions of tunnels between alkali ions lying in the interlayers, since these individual sites are resolved in electron micrographs of micas. An evaluation of the usefulness of one-dimensional lattice fringe images for studying disordered states in crystals is also discussed by comparing them with structure images of corresponding crystals. Intimate intergrowths of different mica polytypes on a scale of tens of ångströms raise questions as to the definition of origins of unit cells and therefore polytypes.

1. Introduction

The structures of the mica minerals are complex and varied, although based on a relatively simple stacking arrangement. There is a sixfold multiplicity for the stacking of adjacent layers, resulting in a large number of possible stacking sequences and thus polytypes (Smith & Yoder, 1956; Ross, Takeda & Wones, 1966; Takeda, 1967; Baronnet, 1975). X-ray diffraction techniques have been a powerful means of determining average stacking sequences and have solved the problems of mica polytypes, but they are not suitable for studying heavily disordered stacking sequences and their variations within a given crystal.

Recently, high-resolution transmission electron microscopy has been recognized as a powerful means for studying structural irregularities in crystals, particularly linear or planar defects, occurring within one or a few unit cells. We have utilized this technique for the study of crystal defects in various oxide crystals (Iijima, 1971). The basis of the technique is that images of crystals taken under critical experimental conditions (focusing, crystal orientation, *etc.*) directly represent an arrangement of relatively heavy atoms, or groups of atoms in a projection of the structure parallel to the direction of the incident electron beam. Such images are called 'structure images' hereinafter.

We previously reported structure images of some minerals (Iijima, Cowley & Donnay, 1973; Buseck & Iijima, 1974; Pierce & Buseck, 1976). One of the advantages of structure images over X-ray diffraction techniques, where observed quantities are averaged over vast numbers of unit cells, is that they allow us to examine local irregularities in crystals at the unit-cell level. This advantage was utilized to study defects and polytypism of enstatites (Iijima & Buseck, 1975; Buseck & Iijima, 1975).

In a previous paper (Buseck & Iijima, 1974) we briefly reported on the imaging of one of the sheet silicates, muscovite, and showed the feasibility of applying structure-imaging techniques to micas.

Mica crystals commonly show streaking in X-ray diffraction patterns. The diffuse streaks are believed to result from stacking disorder. It is of interest to study these disordered micas by high-resolution electron microscopy, in order to obtain further information on mica polytypism and the nature of the disordered layer sequences. We report here the method of observing disordered mica crystals using structure images taken by high-resolution electron microscopy; the usefulness and limitation of one-dimensional lattice fringe images is discussed.

2. Experimental procedure

In order to study stacking disorder of mica layers, it is essential to examine the crystal structure in a direction parallel to the layers. The excellent cleavage along the layers has severely hindered the preparation of specimens where this can be done. For this study, specimens were prepared by sectioning the crystals of micas with a diamond knife in an ultramicrotome. This technique has been successfully applied to studying asbestos (Yada, 1971) and some clay minerals (Lee, Jackson & Brown, 1975). In order to support the mica plate in the microtome, the crystal was embedded in a relatively hard epoxy resin, as is usual for biological-specimen preparation. Although it was rather difficult to make large uniform sectioned films from mica crystals, the crystals were easily fractured into small pieces; large enough thin fragments for our present purposes were obtained. Sections were collected on holey carbon supporting films on a copper grid. Thin crystals were searched and tilted or rotated using a goniometer stage in the electron microscope so as to orient their (0*kl*), (*hhl*) or (*hk̄l*) reciprocal-lattice planes perpendicular to the incident electron beam direction. The structure images were observed with a JEM-100B electron microscope at 100 kV.

Since observations of the structure images are so critically dependent on various experimental factors for imaging and are extremely difficult and time-consuming to obtain, the crystals were also examined with ordinary lattice fringe images obtained by ordinary bright-field illumination. Such images result from simple interferences between the transmitted and diffracted electron beams from systematics which pass through the objective aperture of the microscope. These images generally do not show a one-to-one correspondence with crystal structures, but do show the major periodicities of the lattice. In order to examine only variations in periodicities of crystals, it is much easier to use these lattice images for a quick examination of the crystals.

3. Description of mica and its images

3.1. *Ordered structures*

The ideal structure of mica can be described by two sheets of hexagonally linked silicon–oxygen tetrahedra (*T*) joined together by octahedrally coordinated cations (*O*) to form *T*–*O*–*T* layers. Vertices of the octahedra located at the centers of hexagonal rings of oxygen atoms are occupied by hydroxyl ions. The *T*–*O*–*T* layers are stacked on top of one another with a sheet of alkali metals in 12-fold coordination bonding them together. The upper and lower $(Si_2O_5)_n^{2n-}$ sheets in a *T*–*O*–*T* group are staggered by $\frac{1}{3}a$ (referred to the 1 *M* monoclinic lattice) with respect to each other.

If we assume that the two $(Si_2O_5)_n^{2n-}$ sheets on either side of the alkali-metal interlayer have hexagonal symmetry and are mirror images, then there are six different ways to stack *T*–*O*–*T* layers on top of one another. Such layering sequences form the basis on

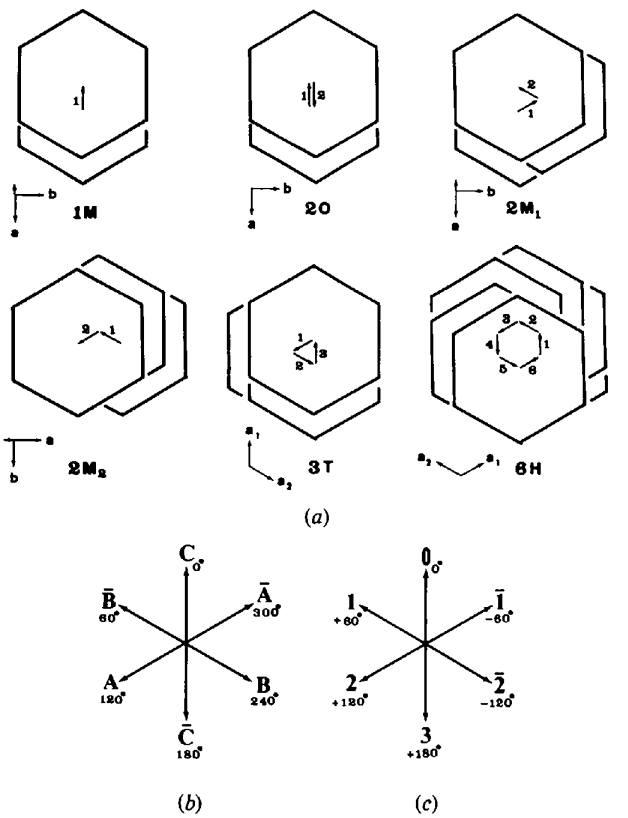

Fig. 1. (*a*) Schematic diagram of mica polymorphs (after Smith & Yoder, 1956). The apices of the hexagons define the sites of the alkali ions in the interlayer sites. The stacking vectors between successive layers are indicated by arrows. (*b*) Designation of six single-layer position symbols of Zvyagin. Arrows indicate direction of the layer stagger of the individual *T*–*O*–*T* layer, referred to the standard mica layer orientation $\bar{C}$ with **a** directed down and **b** to the right. (*c*) Vector stacking symbols of Ross *et al.* (1966). The symbols define stacking angles between adjacent layers.

which Smith & Yoder (1956) originally proposed that theoretically there will be at least six mica polytypes: $1M$, $2M_1$, $2M_2$, $2O$, $3T$ and $6H$. However, Ross *et al.* (1966) found that the $(Si_2O_5)_n^{2n-}$ sheets in naturally occurring trioctahedral micas have a trigonal symmetry due to the displacement of the surface oxygen atoms of the sheets. The trigonal symmetry of the surface oxygen atoms permits the adjacent layers to fit only when the layers are rotated with respect to one another by 0 or $\pm 120°$. Thus, mica polytypes $2M_2$, $2O$ and $6H$ that result from ± 60 or $\pm 180°$ layer rotations are very rare.

For describing the polytypes, it is convenient, following Smith & Yoder (1956), to take two tetrahedral $(Si_2O_5)_n^{2n-}$ sheets and interlayered alkali metals as the basic unit, instead of the T–O–T layer. If this is done it is sufficient only to refer to the alkali-metal sheets for reference purposes. The six polytypes of micas are illustrated in Fig. 1(*a*), where hexagonal networks of alkali metal sheets are represented by hexagons. Arrows are stacking vectors with magnitude $\frac{1}{3}a$.

3.1.1. *Tunnels in mica.* A notable feature of the mica structure is that parallel to [100], [110] or [1$\bar{1}$0] (for the $1M$ setting), there are 'empty tunnels' within interlayers. The tunnels result in regions with lower electrostatic potentials in a projection of the structure along the directions of the tunnels. Thus the positions of these tunnels can be resolved in the high-resolution structure images of the crystals as regions having lighter contrast. In fact, as we describe in the later sections, this has been shown in experimental and theoretically calculated images.

Let us consider the geometric relations between positions of the tunnels in successive interlayers of $1M$. If we look down along the **a** direction, [100] or [$\bar{1}$00] (Fig. 2*a*), there are relatively large tunnels through the structure (shown by broken circles). The positions of these tunnels in the [100] and [$\bar{1}$00] projections are arrayed parallel to [010] and perpendicular to $c \sin \beta$ (Fig. 2*a*). Since the displacement in adjacent T–O–T layers for $1M$ is parallel to [100], the direction of the displacement vector cannot be distinguished in this projection, which is also the one that we observe in the structure image. Therefore, the arrangement of the tunnels in the [$\bar{1}$00] projection is indistinguishable from that in the [100] projection. We schematically represent a sequence of the layers in the [100] or [$\bar{1}$00] projection by circles connected by double lines (Fig. 2*b*). Similar tunnels are also present in projections parallel to [110], [$\bar{1}$10], [1$\bar{1}$0] and [$\bar{1}\bar{1}$0] (Fig. 2*c*,*e*) and their arrangements in the projections in these directions are schematically represented in Fig. 2(*d*) and (*f*) respectively. Since the $-$[110] projection = the [1$\bar{1}$0] projection, and the $-$[1$\bar{1}$0] projection = the [110] projection, the arrangements of the tunnels in the [110] projection and the [1$\bar{1}$0] projection are identical to those in the [$\bar{1}$10] and [$\bar{1}\bar{1}$0] projections respectively.

A possible ambiguity in interpreting experimental mica structure images can arise in the relation between tunnels in successive layers if they cannot be connected by lines orthogonal to the layering (Fig. 2*d*,*f*). In this case the correct orientation can be found from the monoclinic angle $\beta(\sim 100°)$ for the $1M$ trioctahedral mica. For an ideal $1M$ trioctahedral mica the obliquity of the lattice, as projected on a plane perpendicular to [110] and [1$\bar{1}$0] in both the positive and negative

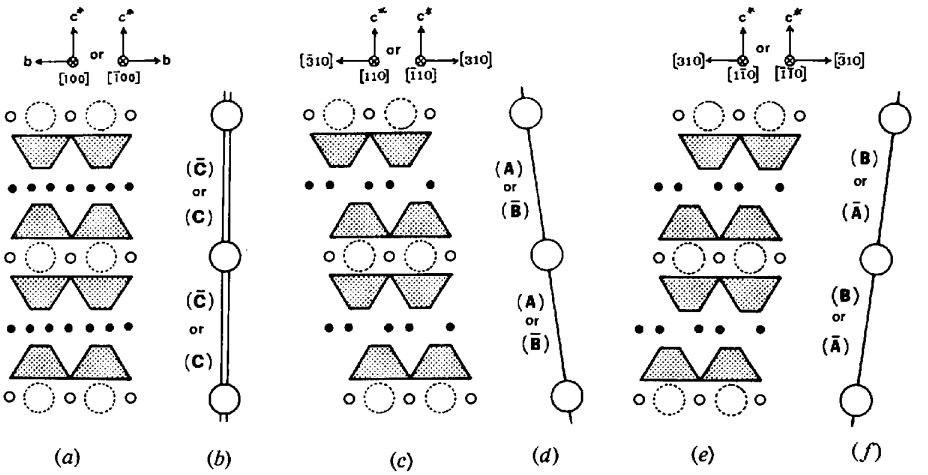

Fig. 2. (*a*) Schematic diagram of mica viewed along [100] or $-$[100] [and thus projected on (100)]. The shaded regions are the sites of the $(Si_2O_5)_n^{2n-}$ sheets, the small black spots are octahedrally coordinated cations, the small open circles are sites of alkali ions in the interlayer sites, and the large dashed circles are the positions of the interlayer tunnels. (*b*) Abstraction of Fig. 2(*a*) showing only the positions of the interlayer tunnels. The lines connecting them are doubled to indicate that they are parallel to **c***. The capital letters indicate orientation, following Zvyagin (1962). (*c*) Schematic diagram of mica viewed along [110] or $-$[110]. The symbols are the same as for Fig. 2(*a*). (*d*) Abstraction of Fig. 2(*c*), analogous to Fig. 2(*b*). (*e*) Schematic diagram of mica viewed along [1$\bar{1}$0] or $-$[1$\bar{1}$0]. The symbols are the same as for Fig. 2(*a*) and (*c*). (*f*) Abstraction of Fig. 2(*e*), analogous to Fig. 2(*b*) and (*d*).

directions, is approximately 98·7°. Consequently, the rows of tunnels that are 8·7° from orthogonal to the layering are the ones that best illustrate the stacking.

3.1.2. *Stacking nomenclature.* For ease of describing stacking sequences of layers, we use the symbols of Baronnet (1975) for labelling the layers. These are based on the stacking vectors shown in Fig. 1(*a*), and combine the interlayer stacking angle symbols of Ross, Takeda & Wones (1966) with the layer positions of Zvyagin (1962). The former indicates the relative rotations in going from one layer to another (Fig. 1*b*) whereas the latter can be used to designate the orientations of the layers (Fig. 1*c*). The standard crystallographic orientations of the micas are indicated by the axes in Fig. 1(*a*); the reference polytype is 1*M*, with **a** directed positively and having a Zvyagin orientation of *C*. Once the orientation of a given layer is specified, all other orientations are fixed and can be indicated by the vectors in Fig. 1(*b*). The relative rotations, however, are 'reset' to 0 at each layer with the rotations to an adjacent layer indicated by the symbols of Ross *et al.* (1966). Using these symbols, the basic structures of the mica polytypes shown in Fig. 1(*a*) are expressed as $1M[0](C)$, $2O[33](C\bar{C})$, $2M_1[2\bar{2}](A\bar{B})$, $2M_2[1\bar{1}](\bar{B}A)$, $3T[222](ABC)$ and $6H[111111](C\bar{B}A\bar{C}B\bar{A})$.

Since the idealized structures of the mica polytypes consist of a sequence of layers which are individually identical with the 1*M* structure, all mica polytypes can be described by a combination of six different layering staggers of 1*M* structure. Using the schematic representation of 1*M* mica shown in Fig. 2, the arrangements of the tunnels and stacking sequences of the layers in the three important projections for each polytype can be derived. They are illustrated in Fig. 3.

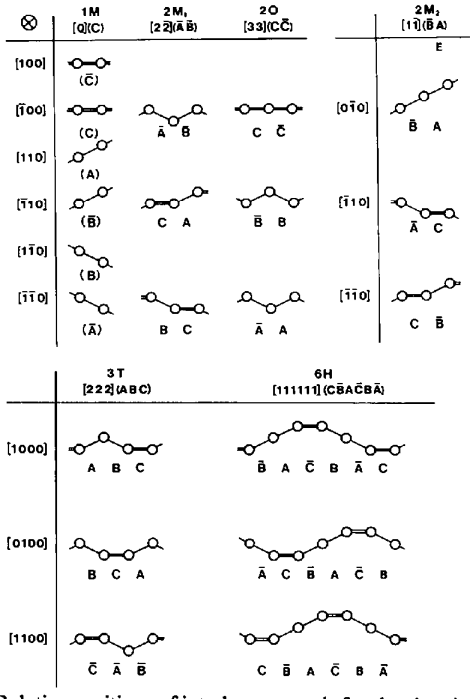

Fig. 3. Relative positions of interlayer tunnels for the six mica polymorphs of Fig. 1, in the projections along the zone axes indicated. In this and subsequent figures, the c^* axis is horizontal. The letter symbols indicate orientation (Zvyagin, 1962). Note **a** and **b** have been interchanged in $2M_2$, thus $[\bar{1}00]$ becomes $[0\bar{1}0]$ *etc.*

The Zvyagin symbols shown in Fig. 3 are designated relative to the orientation of the standard mica layer *C*. For convenience in comparing the orientations of the layers of 1*M* to those in the polytypes, we denote a single Zvyagin symbol for each different projection of 1*M*, although one Zvyagin symbol does not define a stacking sequence. For this reason they are distinguished from the others by parentheses; the same symbols are also used in Fig. 2.

For the 3*T* structure, for which observations are discussed below, there are three different stacking vectors in a stagger of the *T*–*O*–*T* layers, $\frac{1}{3}[1000]$, $\frac{1}{3}[0100]$, $\frac{1}{3}[\bar{1}\bar{1}00]$. The staggers in the [0100] projection are described by a combination of (*B*), (*C*) and (*A*) of 1*M* and can be expressed symbolically as $3T[222](BCA)$.

In general, a single structure image of a crystal provides us only information on its projection. Thus, we cannot distinguish the signs of the stacking vectors if rotation angles between two successive layers are 0 or 180, 60 or 120, 240 or 300° when we look down the *a* axis of one of the layers, referred to the pseudo-hexagonal cell (Fig. 1). Because of this, several polytypes appear to have identical arrangements of tunnels in their images. For example, the images of 1*M* mica crystals in [100] or $[\bar{1}00]$ orientation, *i.e.* $1M[0](\bar{C})$ or $1M[0](C)$, and 2*O* in [100] and $[\bar{1}00]$ orientation, *i.e.* $2O[33](\bar{C}C)$ or $2O[33](C\bar{C})$, appear identical. The complete stacking sequence cannot be determined from one projection alone and we may need two projections (for $\pm 120°$ rotation only) or three (for ± 60, 120, 180°). Unfortunately such stereoscopic observations are not technically feasible at present using high-resolution electron microscopy.

3.2. *Stacking disorder*

If physical disorder in micas results only from mistakes in the stacking of *T*–*O*–*T* layers and no appreciable modifications of the layers themselves occur, the disordered sequences of micas can be described by combinations of the ordered phases shown in Fig. 3. For example, consider a mixture of 3*T* and 1*M*. As mentioned earlier, ideally there will be six different ways to put them together in a sequence. If the $[\bar{1}00]$ direction of 1*M* (hereinafter expressed as $[\bar{1}00]_{1M}$) is coincident with $[1000]_{3T}$ and we look down the $[\bar{1}000]_{3T}$ axis, the projection of the tunnels in a sequence of the two structures will be as shown in Fig.

4(*a*) and can be represented by [––222000––](––*CABCCCC*––). For the case where the $[\bar{1}00]_{1M}$ direction is not parallel to $[1000]_{3T}$, but is rotated clockwise by 60°, for example, around the c^* axis of 3*T*, the arrays of the tunnels for a 1*M* region are the same as those viewing down $[\bar{1}\bar{1}0]$ of 1*M*. This stacking sequence is represented by [––222$\bar{1}$00––](––*CABC*$\bar{A}\bar{A}\bar{A}$––) and the arrangement of the tunnels is shown schematically in Fig. 4(*b*). The same arrangement as shown in Fig. 4(*b*) can also be obtained when there is the 120° clockwise rotation (Fig. 4*c*). In this case the stacking sequence is represented by [––222$\bar{2}$00––](––*CABCBBB*––). This arrangement is an example from the actual image of biotite (*cf.* § 4.5). These two cases (Fig. 4*b*,*c*) cannot be distinguished from one electron micrograph and an additional micrograph taken from the $[0\bar{1}00]_{3T}$ or $[1\bar{1}00]_{3T}$ is required.

4. Results and interpretations

4.1. *Calculated images of mica structure*

In the previous section we described polytypes of micas by noting the positions of tunnels passing through interlayers. Such tunnels, regions with lower electrostatic potentials, have been shown experimentally and theoretically to produce light contrast in structure images (Skarnulis, Iijima & Cowley, 1976). In order to be confident of the intuitive interpretation of the image contrast of mica crystals, it is useful to compare them with theoretically calculated images. Interpretation of the lattice images of crystals can be treated by *n*-beam dynamical theories for electron diffraction. Recently, a computer program for the practical calculation of lattice images based on the multislice method formulated by Cowley & Moodie (1957), has been developed by Fejes (1973), Skarnulis (1975) and O'Keefe & Sanders (1976).

Fig. 5(*a*), (*b*) and (*c*) shows calculated images of $2M_1$ muscovite at three different conditions of focus. The crystal is oriented with [100] parallel to the direction of the incident electron beam; the crystal thickness is assumed to be 50 Å. Structure data for this calculation was taken from Guven (1971). The schematic model for $2M_1$ mica structure and the positions of the tunnels projected on the (100) plane are illustrated in Fig. 5(*d*) and (*e*). In order to be able to see a one-to-one correspondence with the structure from these calculated 'structure images', the image should be taken at an underfocus of nearly 800 Å (Fig. 5*b*), called the 'optimum-focus' condition, and the crystal should be very thin, less than 50 Å. It is evident, as we expected, that the image contrast at the positions of the

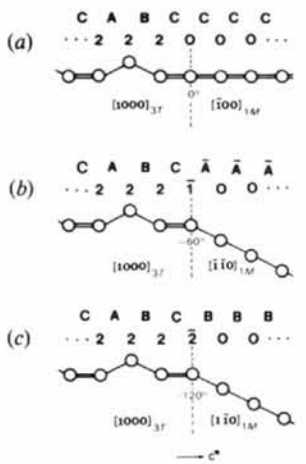

Fig. 4. Sequence of interlayer tunnels for the cases where 1*M* and 3*T* mica are stacked one on top of the other, with (*a*) [1000] of 3*T* and [$\bar{1}$00] of 1*M* parallel, (*b*) [1000] of 3*T* and [1$\bar{1}$0] of 1*M* parallel, and (*c*) [1000] of 3*T* and [1$\bar{1}$0] of 1*M* parallel. In all cases, the viewing directions are parallel to the [1000] of 3*T*.

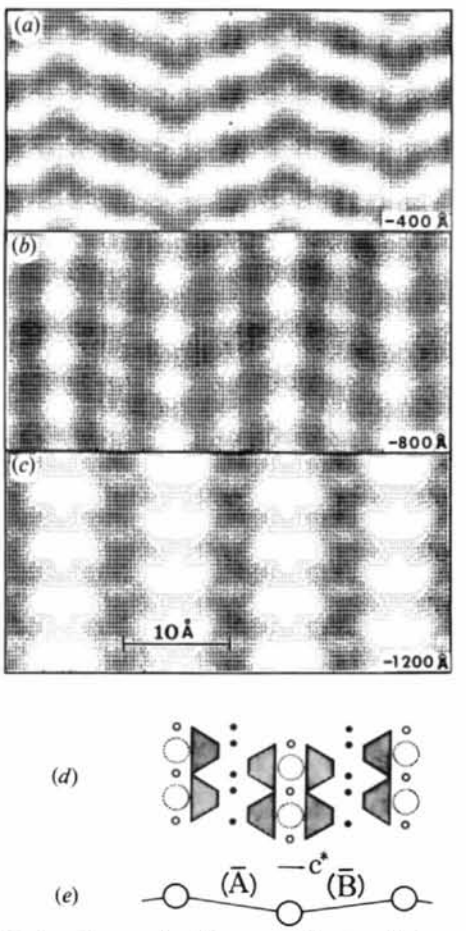

Fig. 5. Calculated images for $2M_1$ muscovite at underfocus values of (*a*) 400 Å, (*b*) 800 Å, and (*c*) 1200 Å. Comparison with (*d*) the schematic structure diagram, and (*e*) an abstraction of relative tunnel positioning, shows that a focus of −800 Å provides the best approximation of the structure. Note that the whitest regions correspond to those of the tunnels. The crystal is oriented with [100] parallel to the viewing direction.

tunnels (connected by lines in Fig. 5*e*) is lighter than elsewhere in the structure. Therefore, it is both valid and useful to describe mica polytypes by referring to the position of the tunnels.

4.2. *Structure images*

4.2.1. 1*M muscovite.* A crystal of muscovite from York, Ontario (ASU No. 1087) 1 cm in width was selected for electron microscopy. Its composition is given in Table 1. Fig. 6(*a*) shows a structure image of the crystal taken at conditions close to the optimum focus. The crystal is oriented with the [110] or [$\bar{1}$10] axis parallel to the incident beam. The inset in Fig. 6(*a*) is an electron diffraction pattern corresponding to the image. By comparison with the calculated images of muscovite (Fig. 5*b*), we can say that each white spot represents the position of a tunnel in the interlayer. Note that the structure of 1*M* in this orientation (Fig. 2*c* and *d*) is the same as that of the right half of $2M_1$ (labelled *C*) shown in Fig. 5(*d*) and (*e*). Fig. 6(*b*) shows a structure image of a different part of the crystal from the same 1*M* muscovite specimen, but the crystal is now oriented with [100] or [$\bar{1}$00] parallel to the incident beam. Note that the arrangements of the white spots are different from those in Fig. 6(*a*) and Fig. 2(*a*) and (*b*).

The arrays of the white spots in Fig. 6(*b*) are shifted across the line indicated by the arrow. This type of planar fault is common in crystals of the 1*M* muscovite that we studied. By referring to Fig. 3, it is seen that this fault results from an insert of a single *T*–*O*–*T* layer structure with [1$\bar{1}$0] or [$\bar{1}\bar{1}$0] oriented parallel to the incident beam direction. In other words the 1*M* layer is rotated by $\pm$120 or $\pm$60°, relative to the host lattice. However, it is known from X-ray studies that the rotation of $\pm$60° is rare in muscovite mica (Ross *et al.*, 1966). If we assume the rotation of 120°, the sequence of the layers in the faulted region would be [––000$\bar{2}$200––](––*CCCBCCC*––) rather than [––000$\bar{1}$100––](––*CCCĀCCC*––), *i.e.* for the case of 60° rotation. In the former case the stacking fault can be described as an intergrowth of one unit cell width of $2M_1$ with [$\bar{2}\bar{2}$](*BC*) or one unit cell width of $2M_2$ with [$\bar{1}$1](*ĀC*).

Table 1. *Electron microprobe analyses of micas*

	Muscovite (ASU No. 1087)		Biotite (ASU No. 325)	
SiO_2	48·6		37·0	
TiO_2	0·18		2·2	
Al_2O_3	33·7		18·9	
Fe_2O_3*	0·64		4·4	
FeO	2·3		15·9	
MnO	n.d.		0·36	
MgO	0·61		9·0	
CaO	n.d.†		0·01	
Na_2O	0·74		0·09	
K_2O	10·0		9·4	
H_2O (by difference)	3·2		2·7	
Number of ions on the basis of 24(O,OH)				
Si	6·53	8·00	5·64	8·00
Al	1·47		2·36	
Al	3·88		1·03	
Ti	0·02		0·26	
Fe Fe^{3+}	0·06	4·34	0·51	5·91
Fe Fe^{2+}	0·26		2·03	
Mn	—		0·05	
Mg	0·12		2·03	
Na	0·19	1·90	0·03	1·85
K	1·71		1·82	
OH	2·9	2·9	2·7	

* Calculated as 80% FeO by weight.
† n.d. = not detected.

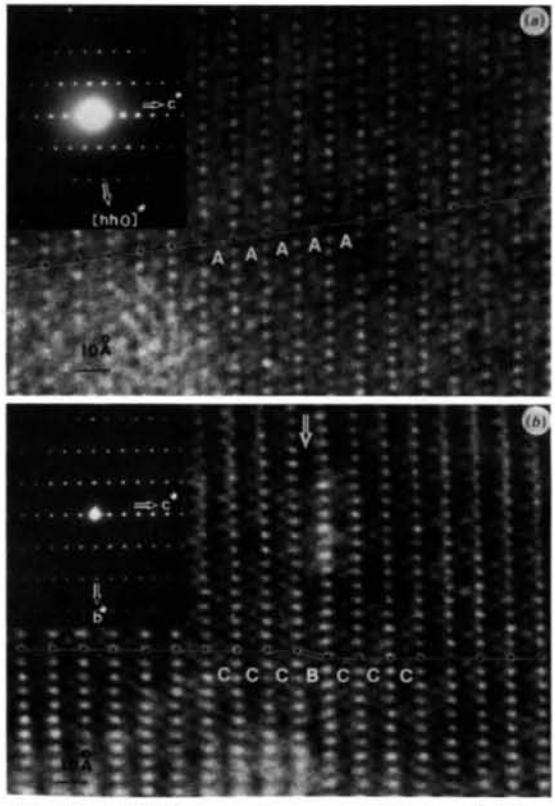

Fig. 6. Bright-field high-resolution structure images of 1*M* muscovite from York, Ontario taken at the optimum focus of about –900 Å, with the corresponding electron diffraction patterns shown in the insets. The white spots correspond to the positions of the tunnels in the interlayers. A line connecting corresponding tunnels has been added to show relative tunnel positioning in the successive layers. (*a*) The [110] zone axis is parallel to the electron beam; this portion of the crystal appears to show ideal stacking. (*b*) Another grain from the same crystal, but with [$\bar{1}$00] oriented parallel to the electron beam. Note the offset of the tunnels at the position of the arrow, indicating a stacking fault. This fault could be described equally accurately as a plate of 1*M* mica, one unit cell wide perpendicular to c^*, which would have been rotated 120° (*B*) or 60° (*Ā*), relative to the rest of the crystal. Although we labelled this as *B* in the picture, these two are indistinguishable from the electron micrograph.

4.2.2. *Biotite.* A crystal of biotite from Mitchell Co., North Carolina (ASU No. 325) several centimeters in width was studied. Its composition is indicated in Table 1. In order to be able to correlate the result of high-resolution electron microscopy with existing structural data, precession photographs were taken of the biotite. The X-rayed sample was taken from the plastic stub that held the sample for ultramicrotoming. The X-rayed sample thus includes the same layers that were studied by microscopy. Mo $K\alpha$ radiation was used together with a camera having a focal length of 100 mm. Photographs of the [010] zone were taken at 60° intervals around **c***.

Fig. 7(*a*) shows a precession photograph. Fraying of the crystal edges from the ultramicrotoming produced the slight circular streaking. There is also some streaking parallel to **c*** in the first and second layer lines. Nonetheless, on average this biotite appears, based on the precession photographs, to have a 30 Å spacing. Intensity distributions in this X-ray photograph definitely indicate that it is predominantly 3*T* (Guven & Burnham, 1967). The high degree of disorder noted in the high-resolution images either is from extremely localized and thus unrepresentative regions, or such disorder does not show up very effectively on the X-ray photographs. We made an attempt to look at many fragments with the electron microscope and, of these, many appeared disordered, but even so these represent a relatively small fraction of the X-rayed volume. However, some fragments (*e.g.* Fig. 7*b*) have electron diffraction patterns similar to the X-ray pattern.

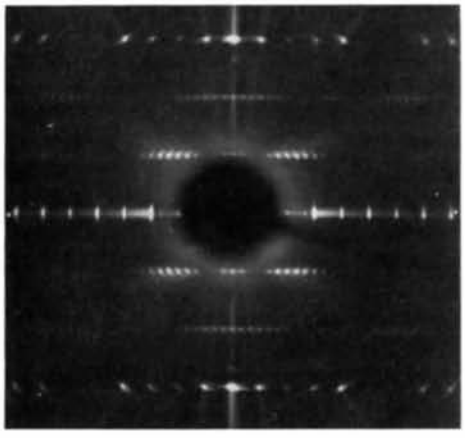

(*a*)

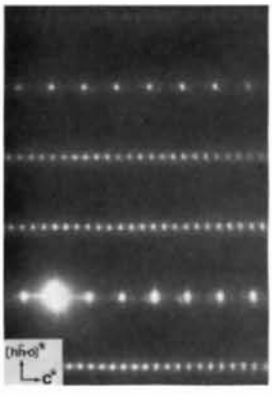

(*b*)

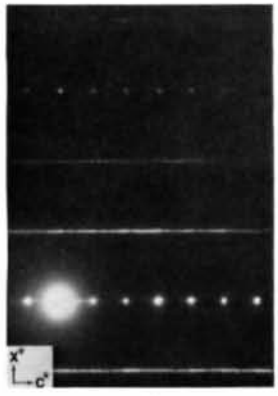

(*c*)

Fig. 7. (*a*) Precession X-ray diffraction pattern of the [010] zone of biotite from Mitchell Co., North Carolina. **c*** is horizontal. Cell dimensions measured from the photograph, assuming a hexagonal cell, are $a = 5{\cdot}35$ (3) and $c = 30{\cdot}3$ (2) Å. Two electron diffraction patterns (*b*) and (*c*) were taken from the same sample as used in (*a*). The patterns in (*a*) and (*b*) are identical and indicate that small regions (several hundred ångströms wide) of the sample are predominantly of the 3*T* type. However, the pattern in (*c*) shows considerable streaking, particularly prominent for reflections having $k = 1$ and 2, suggesting stacking disorder. Note the inhomogeneous distribution of the stacking disorder in this sample.

The crystal in Fig. 7(*b*) has its [10.0] zone axis oriented parallel to the incident beam. The pattern suggests that a major portion of this crystal is of the 3*T* type, space group $P3_112$ or the enantiomorphic $P3_212$. Other grains from the same crystal display considerable streaking (Fig. 7*c*). The streaks parallel to the c^* axis are essentially absent for reflections with $k = 3n$. The origin of the diffuse streaks has been studied extensively in terms of mica polytypism in X-ray diffraction analysis for micas and was explained by random $n(120°)$ layer rotations (Ross *et al.*, 1966).

The degree of streaking varies from fragment to fragment of the crystal. Such variations raise the important question as to what parameters changed during crystal growth to produce both ordered and disordered regions within what is macroscopically a single crystal. The diffraction data of the diffuse streaks (Fig. 7*b*), resulting from the averaged structures, are not adequate to discuss the randomness in the stacking disorder in crystals in detail. For this purpose the high-resolution electron micrographs which are formed by the diffusely scattered beams as well as the Bragg reflections have a great advantage. This is the main theme of the present paper and will be discussed below.

4.3. *One-dimensional lattice fringes*

Using structure images to investigate stacking disorder in micas is useful, but time consuming because of the experimental difficulties. These difficulties include the exact alignment of the crystal and problems of avoiding electron-induced radiation damage. It is therefore desirable to find an alternative, simpler method for studying stacking disorders. This was done by observing one-dimensional lattice fringe images of the thicker crystals, formed by using only systematic (00*l*) reflections (one-dimensional lattice fringes). Neither exact alignment of the crystal nor high magnification for recording the images is required to produce such images (*cf.* Iijima & Buseck, 1976).

One-dimensional lattice images recorded under four different imaging conditions are shown in Fig. 8(*a*), (*b*), (*c*) and (*d*). The images were recorded by tilting the crystal in such a way that the zone axes (determined from the Laue circle) were nearly concident with the direction of the incident electron beam. The thickness of the crystal is much greater than 400 Å. The beams used for imaging, *i.e.* 000 and $l = \pm 1, \pm 2, \pm 3$ are enclosed by a circle (Fig. 8*a*) indicating the position of the objective aperture. The 00 ± 1 and 00 ± 2 reflections are forbidden for the space group $P3_112$ or $P3_212$ for the $3T$ polytype. These reflections, however, are faintly visible and can be explained as resulting from a very slight tilt of the crystal and thus a small deviation in the [1000] zone axis orientation thereby permitting the 'forbidden' reflections. These forbidden reflections are enhanced by multiple diffraction when the crystal thickness is great.

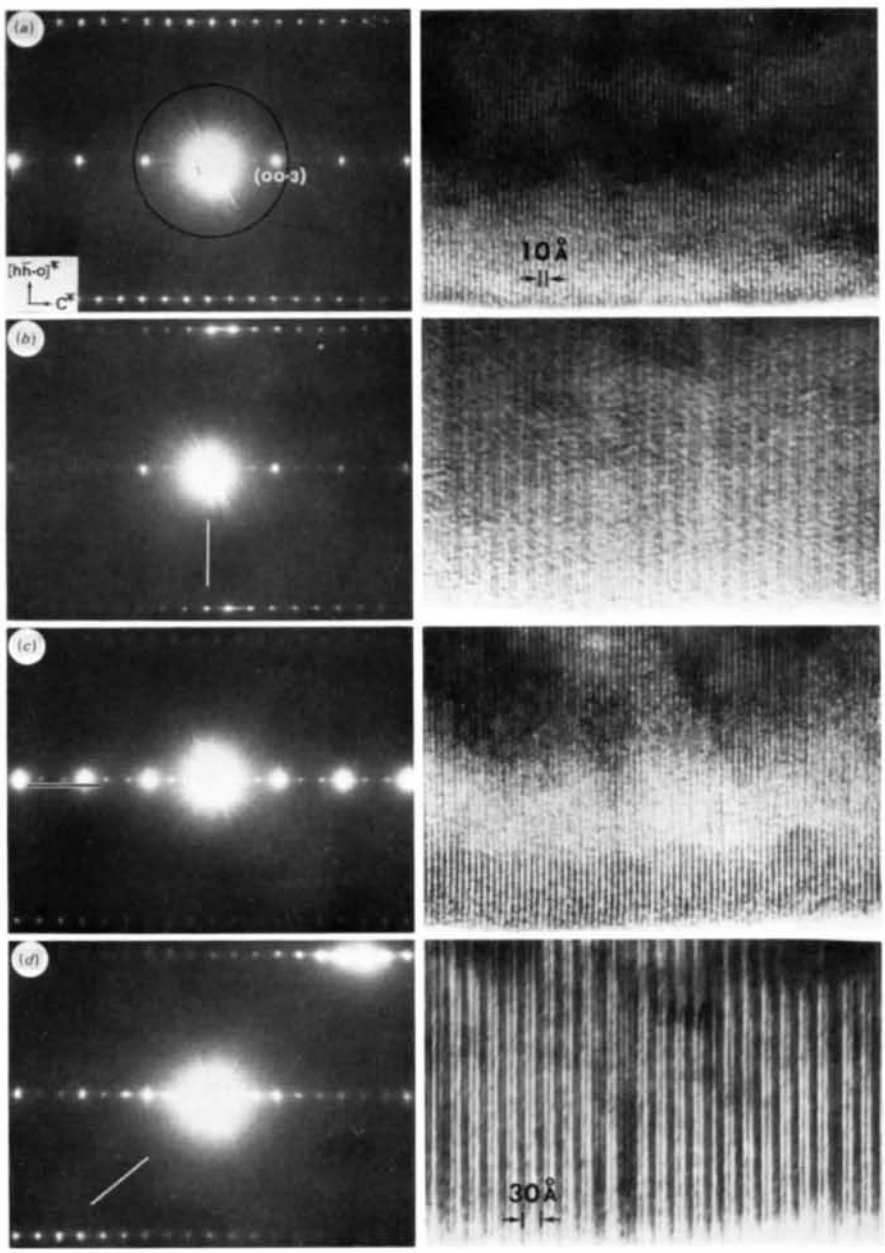

Fig. 8. Electron diffraction patterns and corresponding one-dimensional lattice fringe images for one grain of the same biotite as was shown in Fig. 7. The position of the aperture, shown in Fig. 8(*a*), permits only reflections of the type (00*l*). In (*a*) the crystal is aligned with a crystallographic axis parallel to the electron beam. It has been slightly tilted around crystallographic axes [designated by white lines lying in the (*hhl*) reciprocal-lattice plane in each diffraction pattern (*b*,*c*,*d*)]. The stacking disorder is clearly observed for the diffraction condition in (*d*).

Lattice images for the [10.0] zone axis (Fig. 8*a*) only show the subcell periodicities of 10 Å, the width of a single $T-O-T$ layer. When the crystal is tilted slightly around [12.0] or [00.1] so as to have zone axes [11,0.1] and [12,2.0], respectively, coincident with the electron beam (Fig. 8*b*,*c*), spacings greater than those of the subcell appear, but are not well defined. The crystal orientations were determined by observing the positions of the Laue circles. Finally, if the crystal is tilted so that the center of the Laue circle lies close to but not exactly coincident with one of the principal axes of the diffraction pattern, then the fringes will correctly show the periodicities of the structure. For example, if the crystal is tilted so that [12,2.1] is parallel to the electron beam (Fig. 8*d*), the major 30 Å periodicity of the $3T$ biotite becomes apparent. This effect can be attributed to the fact that the $00 \pm l$ reflections are no longer forbidden; further, such reflections are emphasized by the dynamical diffraction effects. Fig. 8(*d*) also clearly shows irregularities that indicate stacking faults.

Modulations of the subcell periodicities due to the slight changes in the crystal orientation are indicated by the changes in intensities in the electron diffraction patterns. The intensities of the 00 ± 1 and 00 ± 2 reflections, relative to the 00 ± 3 of subcell, vary with the tilt. The major periodicity becomes clearest in the image when the minimum difference in reflection intensity is obtained in the electron diffraction pattern.

4.4. *Comparison between lattice fringes and structure images*

For practical purposes, these observations suggest that it is possible to distinguish mica polytypes to some extent by examining the one-dimensional lattice fringes of a crystal in thicker regions than for structure images, provided the images are recorded under the conditions that were described for Fig. 8(*d*). Fig. 9 shows a bright-field image taken after appropriate tilting of the crystal. The thicker region of the crystal (upper part of the photograph) shows spacings of 10, 20 and 30 Å which may be described in terms of $1M$, $2M$, and $3T$ polymorphs respectively. On the other hand, the image in a thin region (the lower part of the photograph was intentionally overexposed in the enlarger, thereby producing the diagonal line running from upper left to lower right) shows only the 10 Å periodicity, corresponding to the width of a single $T-O-T$ layer. Note that the tilt effect becomes less in a thin region of the crystal.

Fig. 10 shows a structure image corresponding to the area outlined in Fig. 9. As we have seen in Fig. 6(*a*) and (*b*), the white spots in the image at a thin region of the crystal (lower part) represent the positions of the interlayer tunnels. For clarity, the stagger of the white spots is indicated by black and white lines drawn on the photograph. There are three different types of arrays of white spots, or tunnels, across the layers (*cf.* Fig. 3). If we assume that there are no ± 60 or 180° layer rotations as Ross *et al.* (1966) suggested for biotites, we obtain the sequence (layers 1 through 23 in Fig. 10) $[222\bar{2}00222000\bar{2}222222\bar{2}02]$ (*CABCBBBCABBBBB-ABCABACCA*).

With increasing thickness (upper region of the photograph), the white spots become less distinct and the image contrast more complex. This is due to the effects of thickness and a slight deviation from the zone axis orientation for the structure image, so that the image at the thicker region no longer shows a one-to-one correspondence with the crystal structure.

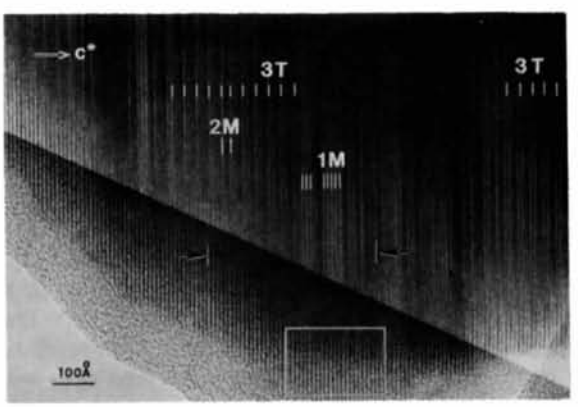

Fig. 9. One-dimensional lattice fringe image of the Mitchell Co. biotite showing plates of several polymorphs intimately intergrown within tens of ångströms of one another. The slanting line is a photographic effect.

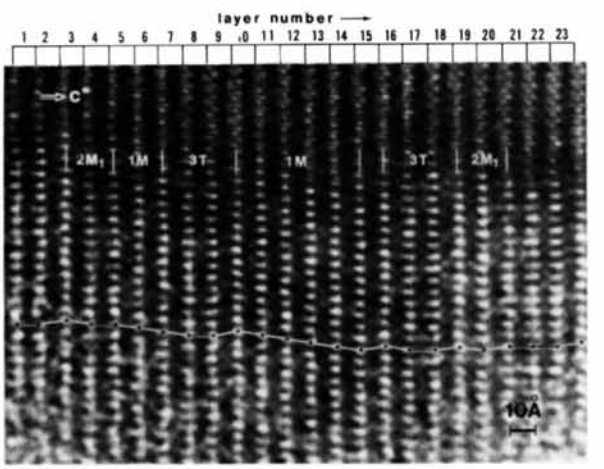

Fig. 10. High-resolution structure image taken from the thin edge (shown by the white rectangle in Fig. 9) of the Mitchell Co. biotite. The tunnels in the interlayer sites are prominent. Their positions are used to define the polytypes. The stacking sequence analyzed for the region indicated by layer numbers 1–23 is given in the text. Procedures for connecting the tunnels by the white (if sloping) or black (if parallel to c^*) lines are also given in the text.

Fig. 11 shows an enlarged one-dimensional lattice fringe image of the area between the arrows in Fig. 9. A portion of this region overlaps with the part of the crystal for which a structure image is shown in Fig. 10. In general, it is not easy to evaluate one-dimensional lattice fringe images in terms of the positions of atoms or groups of atoms in a crystal unless careful image-intensity calculations are made. However, the fringe contrast of the one-dimensional fringe image of Fig. 11 can be correlated with the structure image of Fig. 10 and thereby the stacking sequences can be derived. The sequence of the T–O–T layers obtained from Fig. 10, which is based on the assumption of no ± 60 or 180° layer rotations in this sample, is compared with the one-dimensional lattice images (see Zvyagin notation in Fig. 11). If we coincide the positions of layers having configuration (B) with the positions of the fringes that are the whitest in Fig. 11, it will be found that all the layers designated by (B) correspond nicely to the whitest fringes. Similar correlations can be made for fringes having darkest contrast [see the layer positions of (A)]. Such relations are true for both ordered and, more interestingly, disordered regions. Thus, regions having identical layers will be imaged as having identical contrast in these one-dimensional lattice fringe images. As in the case for structure images, however, the specific contrast relations will vary with the experimental conditions. Thus, it is the relative positions of the fringes rather than the absolute shades of grey that are of significance for interpreting such images.

5. Conclusions

The fact that mica polytypes are common has long been known, although it has only been possible to study them statistically, *e.g.* by X-ray diffraction. In this paper we demonstrate that the details of mica polytypism can be observed by high-resolution electron microscopy. The channels lying between the large interlayer cations appear as areas of light contrast in bright-field images. By noting the arrangements of these interlayer sites the mica stacking sequences are revealed under the assumption that the mica structures that we observed have only 0 and $\pm 120°$ layer rotations. If there were possibilities having ± 60 or 180° layer rotations, the interpretations of the structure images would become more difficult. However, the ambiguity in interpreting structure images of such micas may be solved to some extent by examining one-dimensional lattice fringe images corresponding to the structure images. For example, one of the alternatives for a sequence of $[--0000--](--BBBB--)$ in Fig. 10 is $[--1\bar{1}1\bar{1}--](--B\bar{A}B\bar{A}--)$ which can be regarded as $2O$. The c^* axis of $2O$ mica is double that of $1M$. If such doubling occurs, one-dimensional lattice images of a region of $2O$ taken from a slightly tilted crystal will be modulated, as we showed above, with a superstructure having a periodicity twice that of the subcell. However, no indication suggesting such effects is evident in Fig. 9. We may conclude therefore that a sequence of $--1\bar{1}1\bar{1}--(--B\bar{A}B\bar{A}--)$ does not occur in this crystal.

A correspondence can be demonstrated between structure images and ordinary types of lattice fringe images. It is thus possible to study mica polytypism at other than the high magnifications and critical focusing conditions required for high-resolution imaging. This use of lattice fringe images greatly facilitates electron microscopy for studying micas and their stacking disorder.

One of the interesting results of this study is that several distinct polytypes can occur directly adjacent to one another in apparently coherent intergrowth (*e.g.* $1M$ and $2M_1$ in our muscovite sample, and $1M$ and $3T$ in our biotite). It was confirmed that the state of the disorder due to coherent intergrowths of different polytypes can occur with widths of the single unit cells. If the origins of the mica polytypes result from local compositional variations, particularly of hydrogen content, rather than crystal-growth phenomena, the intimate intergrowths of mica polytypes should be associated with modulation in the chemical compositions of adjacent T–O–T layers. Such local compositional variations cannot be confirmed with available techniques. However, the spacing between successive interlayers, c^*, and the monoclinic angle, β, are dependent on the composition; both of these parameters can be determined from high-resolution structure images of a local area a few unit cells wide. Thus, these images provide the potential not only for indicating polytypes on a scale of 10 Å, but also for eventually yielding approximate compositional data on a comparable scale.

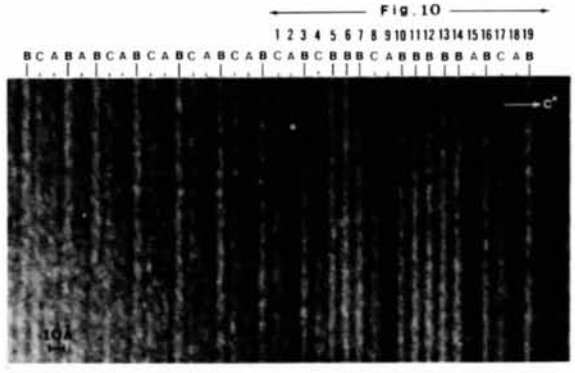

Fig. 11. One-dimensional lattice fringes enlarged from the region between the arrows in Fig. 9. The relative positions of the interlayer tunnels, using the symbolism developed in Fig. 2, and derived by comparing the positions (and then contrast) of the fringes to the structure image in Fig. 10, are shown at the top of the figure. A portion of the layer number shown in Fig. 10 is also designated. Note the whitest fringes corresponding to identical layers are designated by B.

We would like to thank M. Ross, US Geological Survey, for his critical comments to improve this paper, D. Veblen and R. Von Dreele for help with X-ray precession photographs and J. Hunt for help with electron microprobe analysis. We also wish to thank Professor J. M. Cowley for his help. This work was supported by NSF Grant EAR77-00128 from the Earth Sciences Section.

References

BARONNET, A. (1975). *Acta Cryst.* A**31**, 345–355.
BUSECK, P. R. & IIJIMA, S. (1974). *Am. Mineral.* **59**, 1–21.
BUSECK, P. R. & IIJIMA, S. (1975). *Am. Mineral.* **60**, 771–780.
COWLEY, J. M. & MOODIE, A. F. (1957). *Acta Cryst.* **10**, 609–619.
FEJES, P. L. (1973). PhD Thesis, Arizona State Univ.
GUVEN, N. (1971). *Z. Kristallogr.* **134**, 196–212.
GUVEN, N. & BURNHAM, C. W. (1967). *Z. Kristallogr.* **125**, 163–183.
IIJIMA, S. (1971). *J. Appl. Phys.* **42**, 5891–5893.
IIJIMA, S. & BUSECK, P. R. (1975). *Am. Mineral.* **60**, 758–770.
IIJIMA, S. & BUSECK, P. R. (1976). *Electron Microscopy in Mineralogy*, edited by H.-R. WENK, pp. 319–323. Berlin: Springer.
IIJIMA, S., COWLEY, J. M. & DONNAY, G. (1973). *Tschermaks. Mineral. Petogr. Mitt.* **20**, 216–224.
LEE, S. Y., JACKSON, M. L. & BROWN, J. L. (1975). *Clays Clay Miner.* **23**, 125–129.
O'KEEFE, M. A. & SANDERS, J. V. (1976). *Optik*, **46**, 421–430.
PIERCE, L. & BUSECK, P. R. (1976). *Electron Microscopy in Mineralogy*, edited by H.-R. WENK, pp. 137–141. Berlin: Springer.
ROSS, M., TAKEDA, H. & WONES, D. R. (1966). *Science*, **151**, 191–193.
SKARNULIS, A. J. (1975). PhD Thesis. Arizona State Univ.
SKARNULIS, A. J., IIJIMA, S. & COWLEY, J. M. (1976). *Acta Cryst.* A**32**, 799–805.
SMITH, J. V. & YODER, H. S. (1956). *Mineral. Mag.* **31**, 209–235.
TAKEDA, H. (1967). *Acta Cryst.* **22**, 845–853.
YADA, K. (1971). *Acta Cryst.* A**27**, 659–664.
ZVYAGIN, B. B. (1962). *Sov. Phys. Crystallogr.* **6**, 571–580.

Acta Cryst. (1978). A**34**, 719–724

Orientation-Dependent Scattering Factors for Overlap Electron Density

BY A. D. RAE

School of Chemistry, University of New South Wales, Kensington, NSW 2033, *Australia*

(*Received* 31 *January* 1978; *accepted* 20 *March* 1978)

The scattering from the overlap electron density $\psi^*_{i\alpha}(\mathbf{r}-\mathbf{r}_\alpha)\,\psi_{j\beta}(\mathbf{r}-\mathbf{r}_\beta)$ between two orbitals on stationary atoms at $\mathbf{r}_\alpha = 0$ and $\mathbf{r}_\beta$ may be expressed as

$$\chi_{i\alpha j\beta}(\mathbf{k}) = \int \psi^*_{i\alpha}(\mathbf{r}-\mathbf{r}_\alpha)\,\psi_{j\beta}(\mathbf{r}-\mathbf{r}_\beta)\exp i\mathbf{k}.(\mathbf{r}-\mathbf{r}_\alpha)\,\mathrm{d}V = \sum_{l=|m|}^{\infty} i^l \mu_{lm}(k)\, Y^R_{lm}(\mathbf{k}),$$

where $\mu_{lm}(k)$ is an orientation-independent term. $Y^R_{lm}(\mathbf{k})$ are spherical harmonics, where the scattering vector $\mathbf{k}$ is defined in spherical coordinates (k,θ_k,φ_k) and $\theta_k = 0$ corresponds to the direction $\mathbf{R} = \mathbf{r}_\beta - \mathbf{r}_\alpha$. $m = M_\beta - M_\alpha$, where M_α and M_β are the magnetic quantum numbers of the two orbitals defined about the direction $\mathbf{R}$. The general case is described and more detailed expressions are given for overlaps involving s, p_x, p_y, p_z orbitals.

Introduction

The X-ray structure factor for the reciprocal-lattice vector $\mathbf{k}$ may be expressed as $F(\mathbf{k}) = \int \rho(\mathbf{r}) \times \exp(i\mathbf{k}.\mathbf{r})\,\mathrm{d}V_r$, where $k = 4\pi \sin\theta/\lambda$ and $\rho(\mathbf{r}) = \rho_0(\mathbf{r}) + \rho'(\mathbf{r}) + i\rho''(\mathbf{r})$. $\rho(\mathbf{r})$ is the dynamically averaged scattering density at $\mathbf{r}$, $\rho_0(\mathbf{r})$ is the dynamically averaged electron density at $\mathbf{r}$, and $\rho'(\mathbf{r})$ and $\rho''(\mathbf{r})$ are wavelength-dependent contributions.

It is also useful to describe the structure factor as

$$F(\mathbf{k}) = \sum_\alpha f_\alpha(\mathbf{k})\, T_\alpha(\mathbf{k}) \exp(i\mathbf{k}.\mathbf{r}_\alpha),$$

where $f_\alpha(\mathbf{k})\, T_\alpha \exp(i\mathbf{k}.\mathbf{r}_\alpha)$ is the contribution to $F(\mathbf{k})$ from the αth atom whose most probable nucleus position is $\mathbf{r}_\alpha$. $f_\alpha(\mathbf{k})$ can be evaluated from a static model where all nuclei are at their most probable positions. $T_\alpha(\mathbf{k})$ may then be regarded as a thermal